IEEE Access
Multidisciplinary | Rapid Review | Open Access Journal

Received September 7, 2020, accepted September 21, 2020, date of publication October 1, 2020, date of current version October 13, 2020.

Digital Object Identifier 10.1109/ACCESS.2020.3028066

Simulation Research of Multi-Pinhole Collimated L-Shell XFCT Imaging System

YAN LUO, PENG FENG, JING GUO, RUGE ZHAO, PENG HE, AND BIAO WEI
Key Laboratory of Optoelectronics Technology and Systems, Ministry of Education, Chongqing University, Chongqing 400044, China

Corresponding authors: Peng Feng (coe-fp@cqu.edu.cn) and Peng He (penghe@cqu.edu.cn)

This work was supported in part by the National Key Research and Development Program of China under Grant 2019YFC0605203; in part by the Chongqing Basic Research and Frontier Exploration Project under Grant cstc2020jcyj-msxmX0553, Grant cstc2020jcyj-msxmX0879, and Grant cstc2020jcyj-msxmX0362; in part by the Fundamental Research Funds for the Central Universities under Grant 2019CDYGYB019 and Grant 2020CDJ-LHZZ-075; and in part by the Scientific and Technological Research Program of Chongqing Municipal Educational Commission under Grant KJQN201904007.

ABSTRACT Polychromatic source X-ray fluorescence computed tomography (XFCT) is a novel imaging method, which is applied for the diagnosis and treatment studies of early stage cancer. In this paper, we propose a fast multi-pinhole L-shell XFCT imaging system to reduce the scan time and radiation dose, which has potential in detecting lower concentration of contrast agents (gold nanoparticles, GNPs). Two kinds of phantoms –the concentration-phantom 1 and the size-phantom 2 are designed to verify imaging performance for low-concentration and small-size ROI. The scanning processes are simulated by Geant4, and images are reconstructed by Optimized EM-TV algorithm. It is concluded that this imaging system is more sensitive in detecting low concentration GNPs than K-shell imaging system. Simulation experiments show the reconstructed images can achieve the highest CNR both for phantom 1 and phantom 2 with iterating 10 times. The detection limit can reach 0.16% when pinhole radius is 0.08mm.

INDEX TERMS L-shell XFCT, multi-pinhole collimator, CNR, low-concentration, small-size ROI.

I. INTRODUCTION

X-ray fluorescence computed tomography(XFCT)is a novel way to detect early stage cancer, combined X-ray computed tomography(X-CT) with X-ray fluorescence analysis(XRF) [1]–[3]. Grodzins L *et al.* first proposed XFCT [4] in 1983. Then in 1996, Takeda *et al.* introduced the principle of XFCT in detail and measured the distribution of iodine in mice with a synchrotron radiation source [5]. Therefore, the previous experiments were all based on synchrotron radiation source. In recent years, they have turned to conventional X-ray tube source. For example, Cong *et al.* successfully reconstructed the concentration of GNPs from 0.2% to 0.5% by using fan beam X-ray tube source and parallel single-hole collimation [6]. Deng *et al.* used conventional X-ray tube source detected the distribution of GNPs in mouse kidney [7].

However, the bremsstrahlung of X-ray tube source makes the radiation dose relatively large, and most of the current studies are based on K-shell XFCT, which has low detection sensitivity. The imaging sensitivity of the L-shell is 6 times greater than that of K-shell theoretically [8], [9]. Therefore, it is necessary to expand the research on L-shell XFCT to detect lower concentration and decrease radiation dose.

Due to the high sensitivity of L-shell XFCT, it is possible to detect lower-concentration elements; and the incident X-ray energy that excites the L-shell is lower than that of the K-shell. Therefore, the research on L-shell XFCT is significant to low-concentration and low-dose imaging.

This paper proposes a non-rotating multi-pinhole collimated XFCT system that uses fan beam to scan only once, which greatly reduces the scanning time and radiation dose. The system performance is verified by Geant4 software, and it is concluded that this system can effectively detect different concentrations and size ROIs. Compared with the K-shell, for lower concentrations, the reconstructed images quality of the L-shell is better than that of K-shell. At the same time, changing the radius of the collimated holes to optimize the system, it is concluded that 0.1mm is better than 0.08mm for high concentrations; and 0.08mm is better for low concentrations. The minimum concentration of GNPs can be distinguished is less than 0.1% for this system. In the rest of this paper, the proposed method is described in Section II. The experiments and the results are presented in Section III. We conclude this paper in Section IV.

The associate editor coordinating the review of this manuscript and approving it for publication was Hengyong Yu.

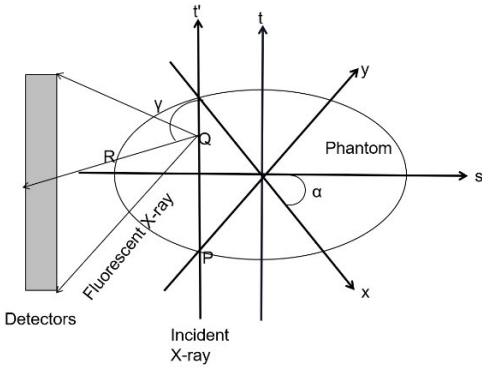

FIGURE 1. Geometry of XFCT.

II. METHOD

In this study, we designed two phantoms to verify the system's performance for L-shell fluorescence detection and XFCT images reconstruction. Phantom 1 is to explore the relationship between the concentration of GNPs and reconstructed images quality, especially for low concentration. Phantom 2 is to explore the relationship between the size of ROIs and the images quality, especially for the small radius. We also set three kinds of pinhole collimators with different size(0.8mm, 1mm, 1.5mm) to illustrate the influence of pinhole size on contrast to noise ratio (CNR). The scanning and detecting process are simulated by Geant4 and images are reconstructed by Optimized EM-TV algorithm [10].

A. XFCT IMAGING THEORY

XFCT can be seen as a stimulated emission tomography, in which a sample is irradiated with X-rays more energetic than the K-shell energy of the target elements of interest. This will produce fluorescence X-rays isotopically emitted from the sample, and the characteristic X-ray can be externally detected for the image reconstruction [9].

we established a coordinate system x-y and a rotating coordinate system s-t (Fig.1). The relationship between s-t and x-y is as follows:

$$\begin{aligned} s &= x\cos\alpha + y\sin\alpha \\ t &= -x\sin\alpha + y\cos\alpha \end{aligned} \tag{1}$$

The process of incident X-rays with an initial intensity of I_0 is divided into three steps: the attenuation process of incident X-rays from P to Q; fluorescence is excited at point Q; fluorescent X-rays reach the detector after attenuation [2], [5]. Then the total flux rate, I, of the fluorescent X-ray reaching the detector is:

$$I = \int_{-\infty}^{+\infty} f(\alpha, s, t)g(\alpha, s, t)d(s, t)\mathrm{d}t \tag{2}$$

where the $f(\alpha, s, t)$ and $g(\alpha, s, t)$ are shown as follows:

$$f(\alpha, s, t) = I0\exp[-\int_{-\infty}^{u} \mu^I(s, t')\mathrm{d}t'] \tag{3}$$

$$\begin{aligned} g(\alpha, s, t) = \mu ph\omega \int_{\gamma m}^{\gamma M}\int_{0}^{+\infty} \mu^F \\ \times (s - b\sin\gamma, s + b\cos\gamma)\mathrm{d}b\mathrm{d}\gamma \end{aligned} \tag{4}$$

Note that the term $f(\alpha, s, t)$ represents the process of incident X-ray reaching point Q, the term $g(\alpha, s, t)$ represents the process of fluorescent X-ray radiated from point Q reaching the detector. α and s variables denote the angle and the translational offset of the incident X-ray, respectively. μ_{ph} is photoelectric linear attenuation coefficient of GNPs. ω is the angle at point Q viewed by detector. γ is the angle between fluorescent X-ray and t' axis, γ^m means the minimum angle, γ^M means the maximum angle.

Therefore, (2) is the function of fluorescent intensity and contrast agent distribution $d(s, t)$. The reconstruction defined as an inverse problem in estimating $d(s, t)$ from the known linear attenuation of incident X-ray μ^I, and fluorescent X-ray μ^F and the detected I.

B. RECONSTRUCTION ALGORITHM

In this study, we used the Optimized EM-TV algorithm, which considered the influence of Compton scattering and apply the reweighted total variation (TV) norm as the penalty function, which obtained images with lower background noise [10]–[13].

$$\begin{aligned} I^{SCA} = \iint_D I_0\exp(-\int_{-\infty}^{Q}\mu^I(s, t)\mathrm{d}s)d(s, t)\mu_{co} \\ \times f_{KN}(E, \theta^{SCA})\int_{\gamma}\exp(\int_{Q}^{R}\mu^F(s, t)\mathrm{d}b)\mathrm{d}\gamma\mathrm{d}t \end{aligned} \tag{5}$$

where θ^{SCA} is scattering angle; μ_{CO} is Compton scattering cross-section; f_{KN} is the Klein-Nishina formula:

$$\begin{aligned} f_{KN}(E, \theta) = \pi r_0^2\sin\theta\frac{1 + \cos^2\theta}{[1 + \alpha(1 - \cos\theta)]^2} \\ \times (1 + \frac{\alpha(1 - \cos\theta)^2}{(1 + \cos^2\theta)[1 + \alpha(1 - \cos\theta)]}) \end{aligned} \tag{6}$$

where r_0 is classical electron radius, $\alpha = E/(m_0c^2)$

$$\begin{aligned} d_j^{k+1} = \frac{d_j^k}{\sum_{i=1}^m h_{ij}^{(XRF)}}\sum_{i=1}^m h_{ij}^{(XRF)} \\ \times \frac{I_i^{(ALL)}}{\sum_{j=1}^n (h_{ij}^{(XRF)}d_j^k + h_{ij}^{(SCA)}S_j^k)} \end{aligned} \tag{7}$$

where

$$I_i^{(ALL)} = I_i^{(XRF)} + I_i^{(SCA)} \tag{8}$$

$$S_j^{k+1} = \frac{S_j^k}{\sum_{i=1}^m h_{ij}^{(SCA)}}\sum_{i=1}^m h_{ij}^{(SCA)}\frac{I_i^{(SCA)}}{\sum_{j=1}^n h_{ij}^{(SCA)}S_j^k} \tag{9}$$

Note that $I^{(XRF)}, I^{(SCA)}$ is the fluorescent projection and scattering noise projection respectively; dj^k, Sj^k means estimated value of concentration and noise of j^{th} pixel after the k^{th} iteration; $hij^{(XRF)}$, $hij^{(SCA)}$ means fluorescent projectio n matrix and the scattering projection matrix.

In reality, the stability and robustness of the algorithm will decrease as the iterations is too large [14]. According to prior

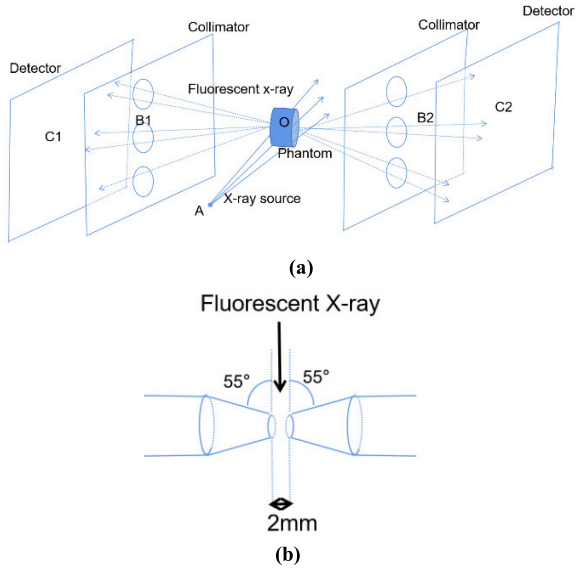

FIGURE 2. (a): Geometry of multi-pinhole collimated L-shell XFCT; (b) Cross-section of single pinhole.

knowledge, the acceleration factor is introduced to improve the convergence of the algorithm.

$$d_j^k = d_j^k - \alpha\omega\upsilon \tag{10}$$

Where α is the gradient descent relaxation factor, ω is the gradient descent scale parameter, υ is the gradient descent direction, which is approximately the partial derivative of the total variation of the image:

$$\begin{aligned}\frac{\partial \|d\|_{TV}}{\partial d_{i,j}} = &\frac{(d_{i,j} - d_{i-1,j}) + (d_{i,j} - d_{i,j-1})}{\sqrt{\varepsilon + (d_{i,j} - d_{i-1,j})^2 + (d_{i,j} - d_{i,j-1})^2}} \\ &- \frac{(d_{i,j+1} - d_{i,j})}{\sqrt{\varepsilon + (d_{i+1,j} - d_{i,j})^2 + (d_{i,j+1} - d_{i-1,j+1})^2}} \\ &- \frac{(d_{i+1,j} - d_{i,j})}{\sqrt{\varepsilon + (d_{i+1,j} - d_{i,j})^2 + (d_{i+1,j} - d_{i+1,j-1})^2}}\end{aligned} \tag{11}$$

where ε is a positive number for fidelity and preventing the denominator from being 0. Normally ε *is an empirical parameter, which is set to a very small number.* Here we set $\varepsilon = 10^{-8}$.

C. IMAGE QUALITY EVALUATION

Here we use the contrast to noise ratio (CNR) [15] as an objective criteria, which is defined as follows:

$$CNR = \frac{|\Psi_A - \Psi_B|}{\sigma_{bk}} \tag{12}$$

where Ψ_A represents the average value of pixels in ROIs, Ψ_B represents the average value of background pixels, and σ_{bk} represents the standard deviation of the pixel values of the background area.

D. MONTE CARLO SIMULATION

In this study, we proposed a novel L-shell XFCT system, which includes X-ray source, a phantom, two sets of multi-pinhole collimators and two sets of detectors, as shown in Fig.2(a). Two sets of detectors are to obtain projections under double incident photons, thereby reducing the radiation dose. The distance between the X-ray source and the center of the sample is 15cm(AO), the distance between the collimator and the sample is 5cm(B1O, B2O), and the distance between the detector and the collimator is also 5cm(B1C1, B2C2). The detector consists of 55 × 185 detector crystals made of CdTe, the energy resolution is 0.5keV, the crystal size is 0.3mm×0.3 mm, and the center distance of the detection crystal is 0.5mm. The multi-pinhole collimator is made of Pb with a thickness of 5mm. There are three pinholes with a radius of 1mm for a set of multi-pinhole collimator. The pinhole is formed by superimposing two cones with a bottom angle of 55°, as shown in Fig.2(b). To avoid overlapping

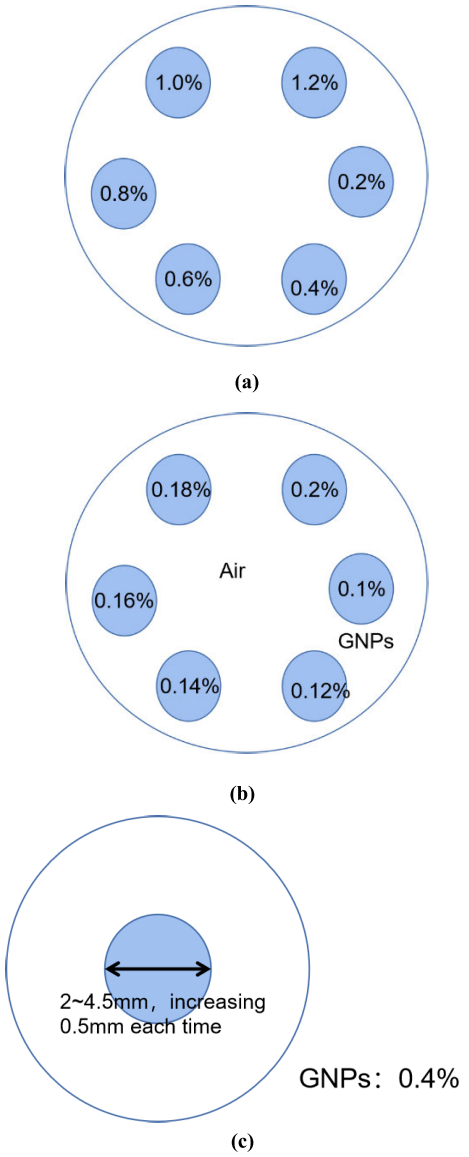

FIGURE 3. (a) Phantom 1-1: to explore the relationship between images quality and GNPs concentrations; (b) Phantom 1-2: reset 1-1 as the low-concentration phantom to improve experiments; (c) Phantom2, to explore the relationship between images quality and ROIs size.

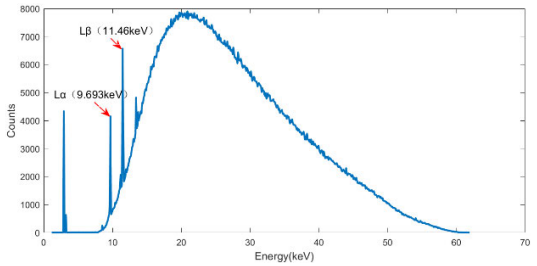

FIGURE 4. Spectrum of X-ray fluorescence.

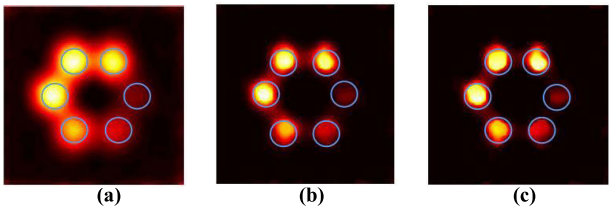

FIGURE 5. Reconstruction image of phantom 1-1. (a): 1 iteration; (b): 5 iterations; (c): 10 iterations.

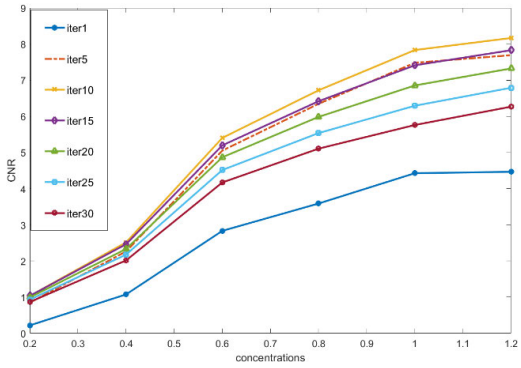

FIGURE 6. CNR of phantom 1-1 under different iterating times.

projections on the detectors, the vertical distance between the holes is 1.5cm. The system is placed in the air.

E. PHANTOM

For *in vivo* imaging, the concentration of the aggregated target material is limited, and the concentration of the corresponding contrast agent (GNPs) is also very low [16]. Therefore, it is necessary to explore the relationship between the concentration and images quality, and the size of the ROIs (Regions of interest) and the images quality. Therefore, this paper designs phantom 1-1(high-concentration phantom): a small cylinder filled with GNPs, with a radius of 1.5mm, and the concentration is 0.2%, 0.4%, 0.6%, 0.8%, 1.0%, 1.2%; when improving the experiment later, we reset the concentration as phantom 1-2: 0.1%, 0.12%, 0.14%, 0.16%, 0.18%, 2.0%; phantom 2: GNPs concentration is 0.4%, the ROI radius is 0.75mm, 1mm, 1.25mm, 1.5mm, 1.75mm, 2mm, 2.25mm. Radius of Phantom 1 and phantom 2 are 2.5cm. The pictorial illustration of phantom 1 and phantom 2 are shown in Fig.3.

III. RESULTS

In this experiment, we simulated the energy distribution of X-ray tube source(tube voltage = 62 keV) in SpekCalc [17],

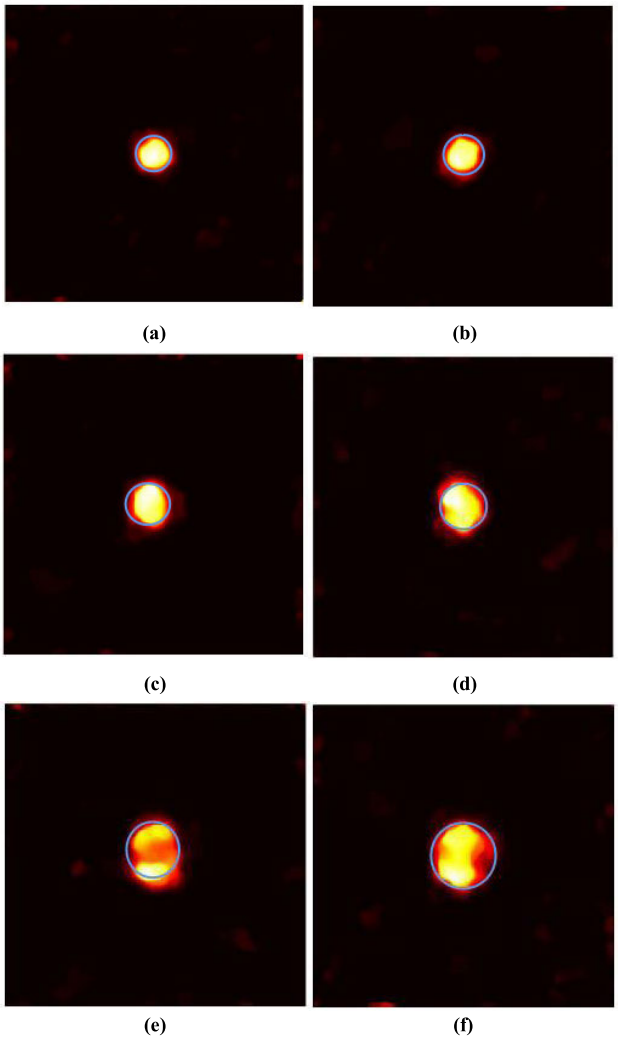

FIGURE 7. The concentration of GNPs is 0.4%, the radius of ROI from (a)-(f):1mm, 1.25mm, 1.5mm, 1.75mm, 2mm, 2.25mm.

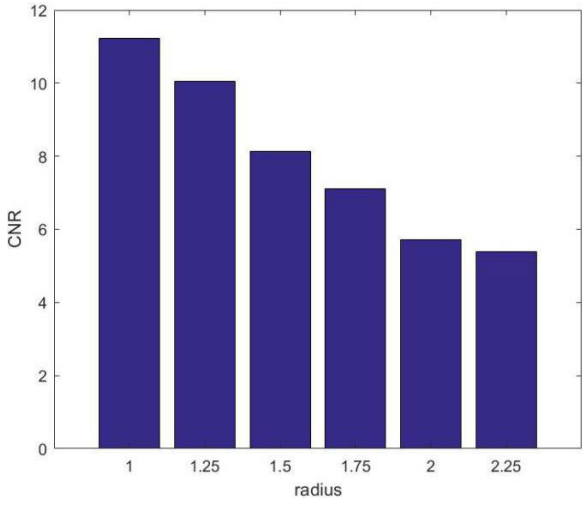

FIGURE 8. CNR of phantom 2.

and the X-ray fluorescent spectrum is shown in Fig.4. The L-edge energy of GNPs are 9.711 keV($L_{\alpha 1}$) and 9.625 keV($L_{\alpha 2}$). Here we used 9.693keV in this experiment

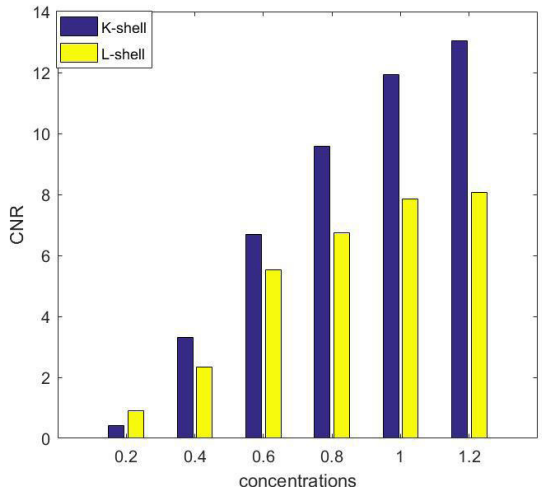

FIGURE 9. CNR of phantom 1-1.

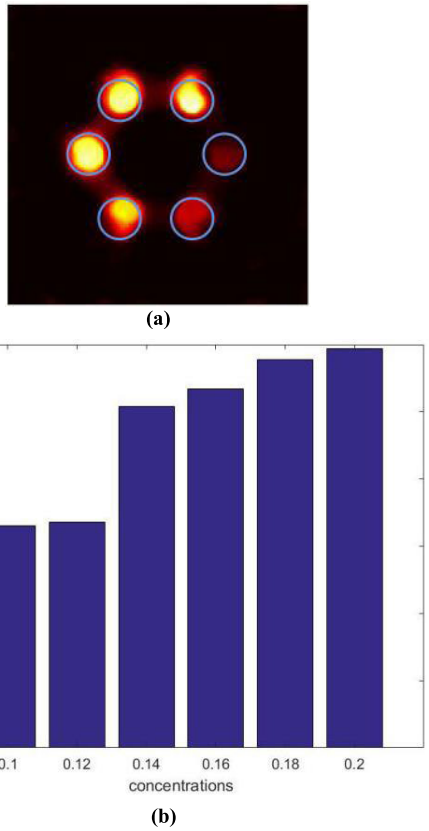

FIGURE 10. (a): Reconstructed image of low-concentration phantom 1-2; (b): CNR of low-concentration phantom 1-2.

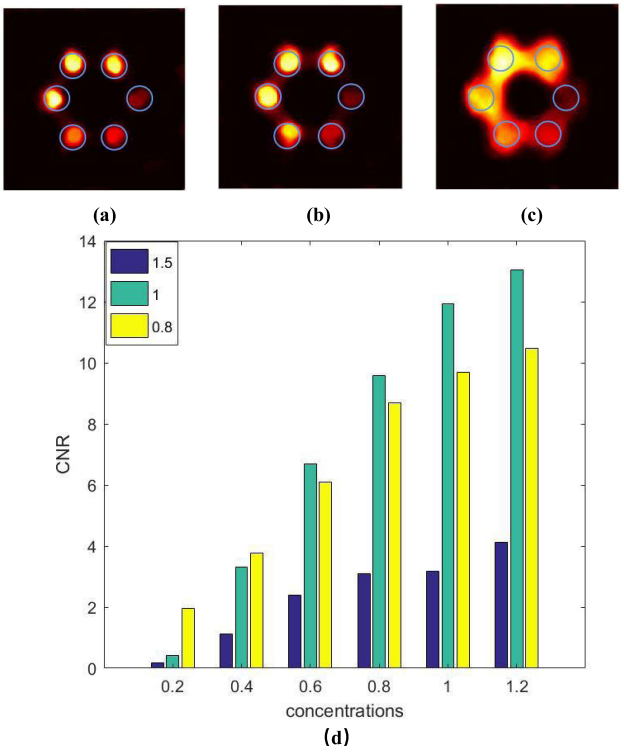

FIGURE 11. Reconstructed images of phantom 1-1 under collimated holes with different radius. (a): The radius of the collimated hole is 0.08 mm; (b) The radius of the collimated hole is 0.1mm; (c) The radius of the collimated hole is 0.15 mm; (d) The CNR of phantom 1 under three kinds of collimated holes.

for the limited energy resolution of detectors. For phantom 1 and phantom 2, the incident X-ray photons are 80 million and 40 million respectively, the effective photons can excite GNPs to produce fluorescence are 72.1 million and 36.05 million respectively. The effective particle ratio is as high as 0.9013, which is much higher than K-shell XFCT [18].

The reconstructed images of phantom 1-1 using the Optimized EM-TV algorithm when the incident X-ray particles are 80 billion are shown in Fig.5: (a)-(c) are the reconstructed images with 1, 5, and 10 iterations, respectively. For 1 iteration image, it is blurred and six ROIs cannot be separated; for 5 iterations image, the ROIs are separated well, uniformity is better, but the boundary between ROI and background is not obvious, especially the ROI with concentration of 0.2%; for 10 iterations image, the boundary is the most obvious and has the best uniformity. To explore the best iterations, we used CNR to estimate every image. Fig.6 shows the CNR of phantom 1-1 under different iterations, which shows that CNR is the largest when iterations equal to 10. Therefore, we reconstruct XFCT images with Optimized EM-TV algorithm and set the iteration parameters equal to 10 (Reconstruction time is 105.043849s, Windows 10, 16GB RAM, AMD Ryzen7 2700X Eight-Core Processor (3.7 GHz), Matlab 2016b).

Fig.7 are the reconstructed images of the phantom 2 when the incident X-ray particles are 40 billion with iterating 10 times. It indicates that when the radius of ROI is 1mm-1.75mm, the boundary of the ROI area is clear; when the radius is 2mm and 2.25mm, the internal attenuation is large and the boundary is blurred. Using CNR for evaluation, according to Rose criterion: ROIs with CNR$\geq$ 4 can be distinguished from the background [13], [19]. As shown in Fig.8, this system has larger CNR when the ROI is smaller, which proves that the system is effective in detecting small object.

The above results show that the proposed system can effectively detect ROI with small size and low concentration. Compared with K-shell image under the same condition,

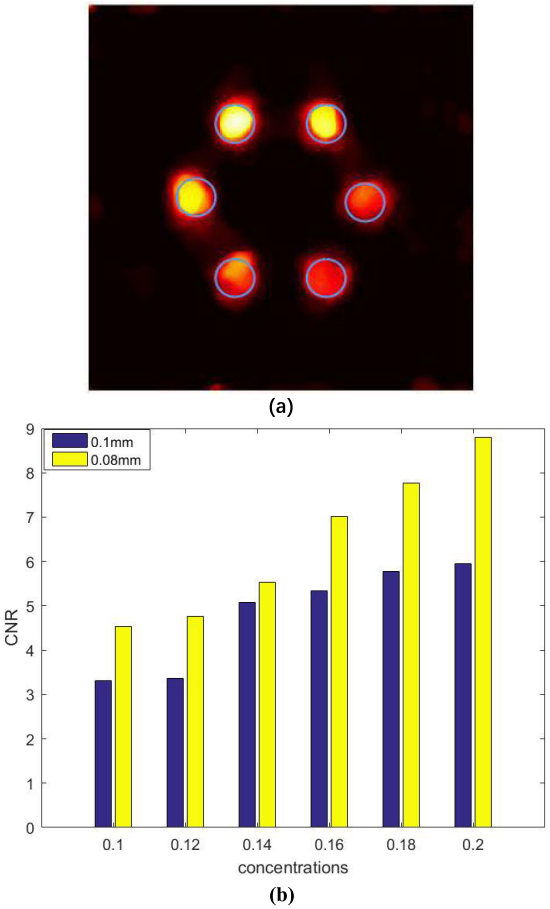

FIGURE 12. (a): The reconstructed image of low-concentration phantom 1-2 (0.1%-0.2%), the collimated pinhole radius is 0.08mm; (b) CNR of low-concentration phantom 1-2.

Fig.9 shows the CNR of L-shell imaging and K-shell imaging, respectively. The CNR of the K-shell is higher than L-shell when the concentration is higher than 0.4%. However, when the concentration is 0.2%, the L-shell imaging outperforms K-shell, showing the potential of L-shell XFCT in detecting lower-concentration contrast agents. For K-shell XFCT, the CNR decreases rapidly as the concentration decreases; In contrast, for L-shell XFCT, the CNR value decreases relatively slow as the concentration decreases, indicating that the concentration has less effect on its image quality for L-shell.

To further explore its ability of detecting low-concentration GNPs, we reset the concentration of phantom 1-1 to 0.1%, 0.12%, 0.14%, 0.16%, 0.18%, 0.2% as phantom 1-2, shown in Fig.3(b). The reconstructed image is shown in Fig.10 (a). The result shows the CNR value is greater than 4 when the GNPs concentration greater than 0.14%, which can be detected in the experiment. In this experiment, the same concentration 0.2% in phantom 1 (high-concentration phantom 1-1:0.2%∼1.2%; low-concentration phantom 1-2 :0.1%∼0.2%) got different results for the different relative position of the 0.2% cylinder placed. It indirectly shows that the fan beam divergence angle affects the scanning results and image quality.

In order to further optimize this system, the radius of the collimated hole is changed for comparison experiments. Fig.11(a)-(c) are the reconstructed images of phantom 1-1 when the pinhole's radius is 0.08mm, 0.1mm, and 0.15mm: at 0.15mm, the ROIs are completely indistinguishable, and the image is extremely blurred; at 0.1mm, the ROIs are separated well, but the uniformity is poor; at 0.08mm, the ROIs are completely separated and have the superior uniformity. Fig.11(d) shows the CNR with 3 kinds of radius. From the Fig.11(d), it can be seen that the radius 0.08mm achieves the highest CNR at low concentrations; at high concentrations, the images quality is best when the radius is 1mm. Fig.12 is the reconstructed image of low-concentration phantom 1-2 with radius 0.08mm. The detected minimum concentration can reach 0.1%, and all of CNR values with radius 0.08mm are higher than those with radius 0.1mm. Therefore, when detecting low-concentration phantoms, the collimated hole radius 0.08mm is a good candidate.

IV. CONCLUSION

In this study, we proposed a fast scanning L-shell XFCT imaging system with 3-pinholes collimator. No translation and rotation are needed during scanning process can reduce its time-consumption and radiation dose. Using Geant4 software to simulate scanning two phantoms proves the feasibility of this system for small-size ROI and low-concentration detection. For phantom 1, the reconstructed image can get the highest CNR and the best image quality when iteration is 10. Compared with K-shell imaging, the image quality of L-shell imaging is better than K-shell in detecting low GNPs concentrations, and the lowest concentration can be detected is 0.16%. In order to further optimize this system, we reset collimating holes' radius to 0.15mm, 0.1mm and 0.08mm, respectively. It's concluded that radius = 0.1mm is a good choice for high concentration experiment(>0.6%), radius = 0.08mm can get the best image quality and the lowest detection limit for low concentration experiment(<0.4%).

In summary, this simulation verified the effectiveness of the proposed XFCT imaging system in detecting small-size ROI and low-concentration GNPs. Furthermore, scanning only once will greatly reduce the radiation dose and exposure time, making this system possible for *in vivo* imaging.

REFERENCES

[1] K. Ricketts, C. Guazzoni, A. Castoldi, and G. Royle, "A bench-top K X-ray fluorescence system for quantitative measurement of gold nanoparticles for biological sample diagnostics," *Nucl. Instrum. Methods Phys. Res. A, Accel. Spectrom. Detect. Assoc. Equip.*, vol. 816, pp. 25–32, Apr. 2016.

[2] L. Li, S. Zhang, Z. Chen, and R. Li, "Full-field fan-beam X-ray fluorescence computed tomography with a conventional X-ray tube and photon-counting detectors for fast nanoparticle bioimaging," *Opt. Eng.*, vol. 56, no. 4, pp. 043106-1–043106-5, 2017.

[3] L. Deng, B. Wei, P. He, Y. Zhang, and P. Feng, "A Geant4-based Monte Carlo study of a benchtop multi-pinhole X-ray fluorescence computed tomography imaging," *Int. J. Nanomed.*, vol. 13, pp. 7207–7216, Nov. 2018.

[4] L. Grodzins and P. Boisseau, "Ion induced X-rays for X-ray fluorescence analysis," *IEEE Trans. Nucl. Sci.*, vol. 30, no. 2, pp. 1271–1275, Apr. 1983.

[5] T. Takeda, M. Akiba, T. Yuasa, M. Kazama, A. Hoshino, Y. Watanabe, K. Hyodo, F. A. Dilmanian, T. Akatsuka, and Y. Itai, "Fluorescent X-ray computed tomography with synchrotron radiation using fan collimator," *Proc. SPIE*, vol. 2708, pp. 685–695, Apr. 1996.
[6] W. Cong, H. Shen, G. Cao, H. Liu, and G. Wang, "X-ray fluorescence tomographic system design and image reconstruction," *J. X-Ray Sci. Technol.*, vol. 21, no. 1, pp. 1–8, 2013.
[7] L. Deng, M. F. Ahmed, S. Jayarathna, P. Feng, B. Wei, and S. H. Cho, "A detector's eye view (DEV)-based OSEM algorithm for benchtop X-ray fluorescence computed tomography (XFCT) image reconstruction," *Phys. Med. Biol.*, vol. 64, no. 8, Apr. 2019, Art. no. 08NT02.
[8] L. Liu, X. Zhou, H. Liu, and N. Ding, "Attenuation correction of polychromatic L-shell X-ray fluorescence computed tomography imaging," *J. Nucl. Sci. Technol.*, vol. 56, no. 5, pp. 376–384, May 2019.
[9] F. Peng, W. Cong, B. Wei, and G. Wang, "Analytic comparison between X-ray fluorescence CT and K-edge CT," *IEEE Trans. Biomed. Eng.*, vol. 61, no. 3, pp. 975–985, Mar. 2014.
[10] S. Zhang, L. Li, and Z. Chen, "Acceleration of the scattering noise model based image reconstruction algorithm for XFCT," in *Proc. IEEE Nucl. Sci. Symp. Med. Imag. Conf. (NSS/MIC)*, Manchester, U.K., Oct. 2019, pp. 1–3.
[11] T. Yuasa, M. Akiba, T. Takeda, M. Kazama, A. Hoshino, Y. Watanabe, K. Hyodo, F. A. Dilmanian, T. Akatsuka, and Y. Itai, "Reconstruction method for fluorescent X-ray computed tomography by least-squares method using singular value decomposition," *IEEE Trans. Nucl. Sci.*, vol. 44, no. 1, pp. 54–62, Feb. 1997.
[12] D. Ma, P. Wolf, A. V. Clough, and T. G. Schmidt, "The performance of MLEM for dynamic imaging from simulated few-view, multi-pinhole SPECT," *IEEE Trans. Nucl. Sci.*, vol. 60, no. 1, pp. 115–123, Feb. 2013.
[13] H. Hsieh and L. Hsiao, "Image reconstructions from limit views and angle coverage data for a stationary multi-pinhole SPECT system," *Tsinghua Sci. Technol.*, vol. 15, no. 1, pp. 44–49, Feb. 2010.
[14] G. T. Herman and D. Odhner, "Performance evaluation of an iterative image reconstruction algorithm for positron emission tomography," *IEEE Trans. Med. Imag.*, vol. 10, no. 3, pp. 336–346, Sep. 1991.
[15] N. Fayed, H. Morales, P. J. Modrego, and M. A. Pina, "Contrast/noise ratio on conventional MRI and choline/creatine ratio on proton MRI spectroscopy accurately discriminate low-grade from high-grade cerebral gliomas," *Academic Radiol.*, vol. 13, no. 6, pp. 728–737, Jun. 2006.
[16] N. Manohar, F. Reynoso, and S. Cho, "TH-AB-209-01: Making benchtop X-ray fluorescence computed tomography (XFCT) practical for *in vivo* imaging by integration of a dedicated high-performance X-ray source in conjunction with micro-CT functionality," *Med. Phys.*, vol. 43, no. 6, p. 3863, 2016.
[17] G. Poludniowski, G. Landry, F. DeBlois, P. M. Evans, and F. Verhaegen, "SpekCalc: A program to calculate photon spectra from tungsten anode X-ray tubes," *Phys. Med. Biol.*, vol. 54, no. 19, pp. N433–N438, Oct. 2009.
[18] J. Guo, P. Feng, and L. Deng, "Optimization of detection angle for pinhole X-ray fluorescence computed tomography," *Acta Optica Sinica*, vol. 40, no. 1, pp. 237–245, 2020.
[19] M. Bazalova, Y. Kuang, G. Pratx, and L. Xing, "Investigation of X-ray fluorescence computed tomography (XFCT) and K-edge imaging," *IEEE Trans. Med. Imag.*, vol. 31, no. 8, pp. 1620–1627, Aug. 2012.

YAN LUO received the B.S. degree from Chongqing University, Chongqing, China, in 2019, where she is currently pursuing the M.S. degree in optical engineering, under the supervision of Prof. P. Feng. Her research interests include the applications of X-ray fluorescence computed tomography and image processing.

PENG FENG received the B.S. degree in mechanical and electronics engineering and the Ph.D. degree in optics engineering from Chongqing University, in 2002 and 2007, respectively, which is one of the most prestigious universities in China. From June 2008 to January 2012, he was a Postdoctoral Fellow of the School of Biomedical Engineering, Chongqing University. He is currently an Associate Professor with the Department of Optoelectronics Engineering, Chongqing University. He has published more than 30 peer-reviewed journal articles as a corresponding author. His interests include computed tomography, compressive sensing, image representation, and biomedical image processing.

JING GUO received the B.S. degree from Henan Normal University, Henan, China, in 2017, and the M.S. degree in optical engineering from Chongqing University, Chongqing, China. Her research interests include the applications of XFCT images and image processing.

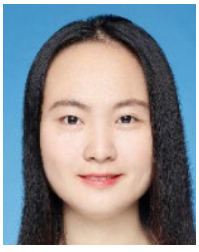

RUGE ZHAO received the B.S. degree from Chongqing University, Chongqing, China, where she is currently pursuing the M.S. degree in optical engineering, under the supervision of Prof. P. Feng. Her research interests include X-ray fluorescence computed tomography and image processing.

PENG HE received the B.S. degree from Nanchang Hangkong University, Nanchang, China, in 2007, and the Ph.D. degree in optical engineering from Chongqing University, Chongqing, China, in 2013. He is also a joint Ph.D. Student with the Virginia Polytechnic Institute and State University majoring in biomedical engineering. He held a postdoctoral position at Chongqing University from July 2013 to June 2015. He was a Lecturer of instrument science and technology with Chongqing University from July 2015 to December 2016, where he is currently an Associate Professor with the Department of Optoelectronics Engineering. He has published more than 30 articles in his research areas. His research interests include X-ray spectral CT imaging, digital image processing, and big data artificial intelligence.

BIAO WEI received the B.S. and Ph.D. degrees from the College of Nuclear Technology and Automation Engineering, Chengdu University of Technology, Chengdu, China, in 1988 and 1996, respectively. He held a postdoctoral position at Chongqing University, Chongqing, China, from October 1996 to May 1999. He was a Lecturer with Chongqing University from June 1999 to November 2004. He is currently a Professor and the Vice Dean of the College of Optoelectronics Engineering, Chongqing University. His research interests include optoelectronics imaging and light energy detection of X-rays, neutrons and visible light, high-resolution optoelectronics imaging detection (sensing) technology with scientific-grade CCD, EMCCD and ICCD digital camera, and optoelectronics image compression coding technology.